Notch Impact Behavior of Oxide Dispersion Strengthened (ODS) Fe20Cr5Al alloy

J. Chao[1], C. Capdevila[1], M. Serrano[2], A. Garcia-Junceda[2], J.A. Jimenez[1], G. Pimentel[1], and E. Urones-Garrote[3]

[1] Departament of Physical Metallurgy, Centro Nacional de Investigaciones Metalúrgicas (CENIM-CSIC), Avda. Gregorio del Amo 8, 28040 Madrid, Spain

[2]División de Materiales Estructurales, Centro Investigaciones Medioambientales y tecnológicas (CIEMAT), Avda. Complutense 22, 28040 Madrid, Spain

[3] Universidad Complutense de Madrid, Centro Nacional de Microscopía Electrónica (CNME), Av. Complutense s/n, E-28040, Madrid, Spain

Abstract

In this paper tensile tests and LS and LT notched Charpy impact tests were performed at the temperature range between -196 and 200 °C on an oxide dispersion strengthened (ODS) Fe20Cr6Al0.5Y_2O_3 hot-rolled tube. The absorbed energy values in the range of high-temperatures of LS notched specimens is considerably higher than those of LT notched specimens; however such values tend to converge as temperature increases. Ductile fracture on the normal planes to RD with delaminations parallel to the tube surface were observed in the temperature range between RT and 200 °C. Delaminations of crack divider type were observed in LT specimens, whereas delaminations of crack arrester type were observed in LS specimens. The yttria particles in the grain boundaries and the transverse plastic anisotropy are the possible causes of that the delaminations were parallel to the tube surface.

Keywords: toughness, mechanical alloying, plastic deformation, oxide dispersion strengthened ferritic alloys

Introduction

Oxide dispersion strengthened (ODS) steels produced by mechanical milling and hot isostatic pressing (HIP) are considered potential structural materials for future fusion reactors since dispersion strengthening appears to be the most promising approach to widening the operating temperature window of the actual ferritic steels [1-2]. The requirements for fusion reactors, sodium fast reactors (SFR), very-high temperature reactors (VHTR), super critical water reactors (SCWR) or other GEN IV nuclear energy systems are different but generic development can be considered for the materials. Due to their high creep rupture strength and excellent swelling resistance, ferritic oxide dispersion strengthened (ODS) materials can be used in several types of reactors and many developments concerning this type of alloys are in progress [3-5]

One of the common key issues to use ODS ferritic steels as a structural material for the advanced fission and fusion nuclear systems are to improve the lower fracture toughness over conventional or reduced-activation ferritic steels [6]. In addition, Alinger et al. [7] reported an anisotropic behavior in the fracture toughness of the hot-extruded MA957 ODS ferritic steels and suggested that the low toughness will be improved by the elimination of stringer-like alumina inclusions from impurities in the source powder. On the other hand, Kasada et al revealed the existence of elongated $M_{23}C_6$ in two types of hot-extruded ODS ferritic steels (Fe–19Cr–4Al–2W–0.3Ti–0.3Y2O3 and Fe–19Cr–0.3W–0.3Ti–0.3Y2O3) containing relatively high concentration (0.05–0.09 wt.%) of impurity carbon [8]. All these results lead us to conclude that the morphology of brittle features in the ODS ferritic steels depends on multiple factors which should not be only the chemical compositions and fabrication process but also impurity level and situation of raw powder that could lead to the formation of undesirable particles. In this paper, the combination of the microstructural factors such as the effective grain size, texture and oxide distribution on notch impact behavior of the Fe20Cr6Al0.5Y_2O_3 hot-rolled tube has been investigated.

Materials and Experimental Techniques

The oxide dispersion strengthened (ODS) Fe19Cr5.5Al0.5Y_2O_3 alloy was commercially available as PM 2000^{TM} and manufactured by Plansee GmbH as reported elsewhere [9-10]. It is a ferritic alloy containing ~20 wt % chromium and 5% aluminum for improving oxidation and corrosion resistance. The detailed chemical composition of the commercial purity PM 2000^{TM} used in this study as determined by X-ray Fluorescence is given in Table 1. After mechanical alloying, the alloyed powder is canned and hot-rolled to form a final 100 mm in diameter tube with wall-thickness of 8 mm.

Table 1. Chemical composition of PM 2000 as determined by XR Fluorescence

	Cr	Al	Ti	C	O	N	Y	Fe
wt.-%	18.60	5.20	0.54	0.04	0.09	0.006	0.391	balance
at.-%	18.50	10.10	0.58	0.17	0.28	0.022	0.228	balance

TEM examination was performed in a JEM-3000 FX transmission electron microscope operating at 200 keV. Cylindrical samples of 3 mm in diameter were cut with diameter parallel to hot rolling direction and mechanically thinned to thickness of ~100 μm. From these discs, TEM samples were electropolished in a TECNUPOL device using 5 pct perchloric, 15 pct glycerol, and 80 pct ethanol as electrolyte, at 266 K with an applied voltage of 20 V. The etchant used to reveal the microstructure in optical microscope was a solution containing 2g $CuCl_2$, 40 ml HCl, 40 – 80 ml ethanol (Kalling Reagent).

Texture measurements were performed in the back-reflected mode by X-Ray diffraction using a Bruker AXS D8 advance X-ray difractometer furnished with an opened Eulerian cradle. Co Kα radiation was employed at a tube current of 30 mA and a voltage of 40 KV. A X-ray spot of 1 mm was used to measure three incomplete pole figures, (110), (200), and (211) in the range of pole distance angle from 0 to 75°. A

measuring time of 10 s per measuring interval in steps of 5° was used. The correction of defocusing was performed using a standard random powder sample of α-Fe. From these pole figures it was calculated the orientation distribution function (ODF) using the series expansion method (l max = 22) and ghost corrected. The sample reference system was orthorhombic, as imposed by the hot rolling process, which is defined by the rolling direction (RD), normal direction (ND) and transverse direction (TD) of the sample. Because of ferrite crystal structure, the orientation density, f(g), was represented in the reduced Euler space ($0 \leq \phi 1, \Phi, \phi 2 \leq \Pi/2$). The sample for texture analysis was taken parallel to the tube surface. This sample was groun and fine mechanically polished with 1 micron diamond paste and colloidal silica (40 nm) to remove the deformed layer.

Microtexture analysis of the as-hot rolled PM 2000 tube specimens was performed by the Electron Backscattering Diffraction (EBSD) technique. EBSD patterns were collected at various locations on cross and flat sections carefully polished with colloidal silica (50 nm particle size) in the final stage. Ultrasonic cleaning process in ethanol at 30 °C is performed in order to remove all the dirtiness from previous steps. The EBSD patterns were generated at an acceleration voltage of 20 kV and collected using a CRYSTAL detector of Oxford Instruments mounted in a SEM JEOL JSM6300. The indexation of the Kikuchi lines and the determination of the orientations were done with the software CHANNEL 5 developed by HKL Technology. The results were represented by means of an inverse pole figure (IPF) maps, which give the orientation of a macroscopic direction with respect to a specific crystal direction. Samples were sectioned according with the scheme shown in Figure 1(b). The rolling direction (RD) is indicated in the figure.

Tensile tests were performed on tensile specimens mechanized parallel to RD of the tube with a gauge length of 22 mm and a diameter of 3 mm. The samples were tested at room temperature at a strain rate of $5 \cdot 10^{-4}$ s^{-1}. The 0.2% yield strength (YS), the ultimate tensile strength (UTS), uniform (ε_u) and total (ε_t) elongation were evaluated from the stress/strain curves. A Class B1 extensometer with a gage length of 10 mm was used to measure the elongation. The compression tests were performed on 6.2 mm side cubic samples mechanized from L, T and S directions (Figure 1(a)) for the study of the anisotropy in mechanical properties. These tests were conducted at room temperature with a strain rate of 5.10^{-4} s^{-1}. Teflon was

used as a lubricant to reduce the frictional contact. The specimen deformation was derived from the displacement of the mobile crosspiece of the machine, subtracting the displacement due to the elasticity of the machine and the compression fixture. The YS and plastic anisotropy coefficient (Rx) in the L, T and S directions were determined according to the following ratios:

$$R_L = \frac{e_T}{e_S};\ R_T = \frac{e_L}{e_T};\ \ R_S = \frac{e_T}{e_L} \quad (1)$$

where e_X (x=L, T, and S) are the engineering strains in the L, T, and S directions according to Figure 1(a).

The orientation of the impact specimens uses nomenclature following ASTM-399 standard by two letters, the first letter designates the direction normal to the crack plane and the second letter designates the direction parallel to the striking direction (Figure 1(a)). L (longitudinal) direction is parallel to the rolling direction RD, T (transverse) is parallel to TD (transverse direction) and S (short transverse) direction is parallel to ND (normal direction). Charpy specimens of 55x6.2x6.2 mm^3 with a V-notch of 1.25 mm in depth were machined in the LT and LS orientation. These reduced-section Charpy specimens were subjected to impact energy of 147 J and velocity at the contact instant of 5.4 m s^{-1} in the range of temperatures between -196 °C and 425 °C. The ductile to brittle transition temperature (DBTT) was determined for impact energy equal to one-half of the difference between the respective lower and upper shelve (USE) energies. For LT specimens the DBTT for 0h, 50h, and 500h aging treatments was of 0 °C, 30 °C and 110 °C respectively whereas for LS specimens was of -10 °C, 0 °C and 180 °C. The samples were heat up in a furnace with a thermocouple welded. Once the temperature is reached, the impact test is performed.

Results

Microstructure of as-rolled samples

Figure 2(a) and (b) shows the microstructure after hot-rolling in the LT and TS planes, respectively. The microstructure consists of fine (~0.5 μm) grains of ferrite. The grains were elongated in RD direction, with an almost equiaxial section in TS plane. The microstructure indicates that the hot-rolling temperature is high enough for recrystallization to have occurred with possibly a little grain growth.

Texture analyses point out the existence of a preferential orientation of <110> along the rolling direction. Moreover, there exists another less strong crystallographic orientation of the ferritic grains, being <100> in the direction perpendicular to the last rolling direction. The phi (2) = 45° section of the Euler space, using Bunge´s angular system, **corresponding to TS-sample** are given in Figure 2(c) and they confirm a strong incomplete α-fiber texture (RD||<110>) with a dominating {001}<110> component, i.e. the crystallographic plane (100) is parallel to the sheet tube surface (section 1 or plane LT in Figure 1(b)).

Microtexture analyses were carried out by EBSD analysis in LT, TS and LS planes. The inverse pole figure (IPF) maps obtained are shown in Figure 3. This figure illustrate the IPF maps of the samples 1, 2 and 3 schematically indicated in Figure 1(b) indicating the <UVW> directions parallel to the sample reference system (X,Y and Z directions). The results indicate that the high angle grain boundaries are well defined, which is also consistent with a recrystallized microstructure. Furthermore, texture analyses reveal that more than 80% of indexed grains present the <110> direction parallel to the rolling direction, i.e. the presence of (110) planes in TS plane is the majority. No {100} cleavage planes were detected in TS plane. This texture is typical of body centered cubic materials deformed by either extrusion or rolling. It is clear from Figure 3(a) that ND || <100>, i.e. (100) plane is parallel to the sheet tube surface (indicated by section 1 in Figure 1(b)). Figure 3(b) indicates that RD || <110>, meanwhile Figure 3(c) shows that the RD plane not only contains the <110> direction but the <111> also. Therefore, it could be concluded that the as-received microstructure presents a strong texture with RD || <110> and ND || <100>. These results are consistent with texture analysis shown in Figure 2(c).

Moreover, Figure 3 indicates that grain morphology presents an elongated shape in the RD direction and an almost equiaxial shape in TS plane. The mean ferritic grain size and the Vickers hardness data obtained on

the three sections are shown in Table 2. Because of the anisotropic grain size, the grain aspect ratio (GAR) values were calculated. GAR value illustrates the degree of elongation since GAR = 1 stands for a sphere. It is calculated by the ratio between the major axis upon the minor axis lengths, and the values for the LT, LS and TS planes are listed in Table 2. More precisely, the grains are quite elongated in the LS and LT sections, i.e. the grains are elongated in the rolling direction. Moreover, a quasi-equiaxial grain size is obtained in TS section where an average diameter smaller than 1 μm is measured. Hardness does not vary significantly in the different sections.

Table 2. Mean ferritic grain size, GAR values and Vickers hardness data for PMT samples

Samples	Section	Mean Length (nm)	Mean Width (nm)	GAR	HV
PMT	LS	1517 ± 656	438 ± 233	3.5 ± 0.3	327 ± 3
	TS	808 ± 127	719 ± 62	1.1 ± 0.3	337 ± 2
	LT	1734 ± 553	431 ± 100	4.0 ± 0.6	330 ± 3

TEM observations revealed areas with arrays and tangles of dislocation as well as dislocation free areas (Figure 4(a)). The reinforcement particles consist of $Y_3Al_5O_{12}$ garnet (YAG) and $YAlO_3$ perovskite (YAP) phases which were determined using HRTEM, XRD and EDX methods (Figure 4(b)). That ODS particles with sizes ranging from 3 nm to 40 nm are mainly located at the grain boundaries as it is shown in Figure 5(a) for TS plane and Figure 5(b) for LS plane. The results obtained are consistent with those reported by Klimiankou et al [11-12] as result of detailed studies with conventional TEM and energy filter TEM (EFTEM) measurements. Besides those fine ODS particles, numerous large inclusions with complex compositions were found in the sample, which are preferentially forming considerably large stringers in LS plane (Figure 5(c)). The investigations showed those stringers are formed by large γ-Al_2O_3 inclusions as well as complex γ-

Al_2O_3/Y–Al–O impurities, which may additionally enclose smaller Ti(C,N) particles [13]. It was not detected equivalent oxide formations in the TS plane.

Tensile and compression tests

Figure 6(a) shows the evolution of strength (YS and UTS values) and elongation (ε_u and ε_t values) derived from tensile tests at temperature range of –60 °C to 300 °C. The difference between yield strength and tensile strength is maintained similar with increasing test temperature, although slightly bigger differences are observed for temperatures tested at 150 and 300 °C, which indicates a substantial work-hardening in all the whole range of temperatures tested with a tendency to increase as testing temperature is increased. On the other hand, total elongation at fracture decreases as temperature increases in the temperature range between -60 °C and 150 °C. At temperature range between 150 and 300 °C, the value of ε_t is maintained constant. Regarding the uniform elongation no substantial differences are observed with the testing temperature in the whole temperature range analyzed. On the other hand, Figure 6(b) shows the evolution of YS and R_X (X=L, T and S) obtained from compression tests at RT. The results clearly indicate the plastic anisotropy of the material for L and T test directions. Same plastic deformation in L and T direction is obtained since the value of R_S is close to 1. However, the low values of R_L and R_T indicate that plastic deformation in S-direction is considerably higher than that in T and L directions, i.e. when the material is axially deformed in L or T directions it tends to deform in plane strain conditions in LS or TS planes respectively.

Charpy impact analysis

Figure 7 shows the Charpy impact energy results for the LT and LS notch configuration presented in Figure 1 with the corresponding fractographic surfaces (in TS plane). Figure 8 illustrates the evolution of the impact load (P) and deflection (u) during the impact test at RT, 75 and 150 °C in the LT and LS samples using an

instrumented Charpy impact test. As a general comment, the results shown in Figure 7 indicate that the values of absorbed energy in the range of high temperatures of LS specimens is considerable higher than those of LT specimens; however, the lower shelf energy does not vary much with the orientation of the notch. This measuring method might not be sensitive enough to detect small differences in the energy absorbed.

Regarding LT specimens (Figure 7(a)) it is clear that for temperatures ranging from -196 to -80 °C , the fracture presents a zigzag morphology on planes tilted ± 45° with respect to notch plane, which is consistent with a cleavage fracture process along (100) planes. No delaminations have been detected in this temperature range. For testing temperature ranging from -30 to 220 °C, the fracture presents a ductile aspect with delaminations parallel to the surface. The appearance of splitting surface presents a macroscopically brittle aspect. The number of delaminations decreased as testing temperature increases (Figure 9).

EBSD analysis was used to investigate the phenomena underlying the splitting in LT samples. Figure 10 illustrate the analyses performed in a plane parallel to LS plane of LT samples fractured at RT which present certain degree of delamination. Figure 10(b) illustrates the misorientations ($\Delta\theta$) measured across the crack between the numbered grains of every pair. It indicates large misorientations across the crack. Thus, crack propagates along the grain boundaries during the delamination, which is consistent with different Euler angles of neighbor grains across the crack (Figure 10(a)). The kernel map also show certain amount of plastic deformation accumulated in the crack tip.

Regarding LS samples, (Figure 7(b)) similar fracture behavior in samples tested at temperatures between -196 °C and RT is observed. In this sense, a macroscopically brittle fracture that propagates by forming 70° respect to the notch is observed (Figure 11). Sometimes the fracture bifurcates from the both sides of the notch tip. Although these fractures present a brittle aspect, they cannot be classified as cleavage fracture nor as pure intragranular fractures, but a mixture of intergranular facets with ductile steps. At temperatures above RT, the fracture presents the same morphological features that those for LT samples. For instance, samples tested at 100 °C, the appearance of the fracture is ductile with the formation of

delaminations parallel to the notch base. Finally, sample tested at 200 °C present a ductile fracture without delaminations.

Some cracks were selected on LT samples fractured at -196 °C for EBSD analysis. Figure 12(a) shows the Euler angles and kernel maps on the LT plane for the LT sample fractured at -196 °C. The kernel average misorientation map shows where the maximum average misorientations are concentrated which is a good indication for where plastic deformation is concentrated. Figure 12(b) shows the IPF and grain boundary map. The crack path forming an angle of 70° with the notch was investigated. The misorientation analyses across the crack between certain pair of grains at both sides of the crack were obtained. It indicates very low misorientations ($\Delta\theta$<10°) across the crack. Thus, one possible crack propagation path is across the grains, which is typical of cleavage fracture. However, the kernel map shows a certain concentration of plastic deformation in the tip of the crack, which is consistent with the above mentioned observation of fractures which present a macroscopically brittle aspect.

As testing temperature increases, the ductile component of the fracture is more evident as it is shown in Figure 13. This figure shows the IPF, grain boundary and kernel maps of LS plane of a LS sample tested at 100 °C. It could be concluded from this figure that crack progress with a considerable amount of plastic deformation and transversal to RD, which is consistent with previous works on laminated structures reported by Kimura and co-workers [16].

Discussion

The FeCrAl ODS alloy examined in this work, in a similar manner to thermomechanically treated steels [14,15,16], laminates [17] and laminated composites [18] that were processed through rolling, exhibit the presence of delaminations parallel to RD [17,19]. In all these cases, the existence of splitting has been attributed to inhomogeneities in some microstructural features. When weak interfaces are present parallel to the longitudinal direction of the impact test bar, the interaction between the weak interfaces and the stress field that is generated by the localized plastic constrain at the notch and/or the crack tip can cause

splitting. There are two basic geometries termed “crack divider” and “crack arrester”. In the case of a delamination type crack divider (LT specimens), the delaminations divide the specimen thickness in as many sub-specimens as delaminations. This causes a relaxation of the stress triaxiality state at the notch tip towards a biaxial stress state. In the lower shelf energy the stress state at the advancing crack tip determines the magnitude of fracture toughness, which increases with decreasing stress triaxiality state, therefore, delaminations produce a decreasing in the DBTT. However in the upper shelf energy in which ductile fracture occurred, the size of the plastic zone ahead of a growing crack is proportional to the thickness of the ligaments between delaminations. Therefore, the higher the delaminations number, the thinner the ligaments are. Since the plastic strain extension prior to fracture contributes significantly to the absorbed energy, the energy required for shear fracture will decrease with increasing in delaminations number. Therefore the effect of the delaminations of the crack divider type is to decrease both the DBTT and the values of absorbed energy in the upper shelf energy.

On the other hand, the toughness values for the LS orientation are ascribed to the crack arrester delaminations type. The delamination causes a strong decrease in the stress intensity at the tip of the 90° bifurcated crack, of about one half of that of the crack immediately before delamination. For further plastic strain it is necessary to reinitiate the fracture across the unnotched ligament. Moreover, it is possible that no fracture occurred during the test. This causes, as it was observed, an apparent high toughening (Figure 7(b)). It is noteworthy that values of absorbed energy strongly depend on the position of the potential delaminations regarding to the crack tip since the strength of the “unnotched beam” is proportional to the thickness times the square of the height of the uncracked ligament. It is the reason for which high dispersion in the values of absorbed energy was observed in Figure 7(b) for high temperatures.

It has been reported above for both LT and LS notched specimens that intergranular delaminations occur along of parallel planes to the tube surface. Nevertheless, we could not find inhomogeneities in the microstructural analysis performed in the TS plane that could explain the existence of delamination of crack arrester type for LS specimens and crack divider type for LT specimens. According with the results shown in Figure 2 and listed in Table 2, the grain morphology is quasi-equiaxed in TS plane, presenting a grain size

with a GAR=1.1±0.3 and an average diameter of 0.8±0.1 μm. The decoration of the grain boundaries with oxide particles is also very clear (Figure 5(a)), but unlike what happens in the LS plane (Figures 5(b) and 5(c)) the presence of stringers that could recombine with those of LS plane to produce weak planes parallel to the tube surface has not been detected. Regarding the above texture analysis, it was concluded from Figures 2(b) and 3(b) the abundant presence of (110) planes in the TS and LS planes, meanwhile the (100) planes, i.e. the cleavage planes are parallel to LT plane and then normal to the notch plane for LT and LS specimens. However no delamination was produced by cleavage but intergranular fracture. On the other hand, in a Charpy test, the principal stress component after strike is σ_L. The other two stress components σ_T and σ_N arise by the localized plastic constraint at the notch tip. The values of the stress components to 0.395 mm from the notch tip, which is the place in that a maximum value of σ_L is reached, are calculated following the Hill's theory [20] for an anisotropic Charpy specimen using the Brozzo and Buzzichelli's expressions [21]. In Table 3 are presented the values of stress components and the corresponding isotropic values for comparison.

Table 3. Values of the stress components to 0.395 mm from the notch tip

NOTCH ORIENTATION	σ_L/σ_{ys}	σ_T/σ_{ys}	σ_S/σ_{ys}
LT	2.41	1.17	1.74
LS	3.13	2.42	1.52
Isotropic LT	2.26	1.10	1.68
Isotropic LS	2.26	1.68	1.10

From the values in Table 3 it is evident that delamination parallel to the tube surface are predicted in LT specimens, but for LS specimens it is predicted in disagreement with experimental results, that delaminations would run parallel to LS plane.

Figure 14 shows a schematic illustration of the splitting in both LT and LS samples, with the corresponding orientation of TS plane regarding the L, T and S system (Figure 1). In a Charpy test, the main stress component after the strike is σ_y. The other two stress components, σ_x and σ_z, are generated by the localized plastic constrain at the notch and/or the crack tip and of lower magnitude than σ_y. The splitting in LT and LS samples could be explained on the basis that the plastic deformation in S-direction (Figure 6(b)) is considerably higher than in T-direction. Therefore, the plastic constrain in S-direction would lead to an increase of σ_x in the case of LT samples, and of σ_z in the case of LS sample that would cause the distribution of cracks found experimentally. Those delaminations are similar to these found under crack-divider and crack-arrester basic geometries. Moreover, the weak interfaces between second phase, such as the Y-Al-Ti oxides located in the grain boundaries aligned to the RD (Figure 5), can also enhance delamination [22-23].

One possible reason why delaminations are produced parallel to the tube surface in the LT and LS samples might be related to the mechanism of deformation associated with the texture <110> of the material. It has been observed when the material uniaxially deforms in the directions L or T that the material does not axisymmetrically but it tends to deform under plane strain conditions in the LS or TS plains, respectively. Furthermore it has been reported [24-26] that BCC polycrystalline materials with texture <110> under uniaxial tensile stress in such <110> direction the following effects occur:

1- The material does not axisymmetrically deform but tends to deform by plane strain. This is an extension of what has already been demonstrated by Hosford for the case of a single crystal [27].

2- As a result of this, tensile stresses in (100) planes and compression stresses in (110) planes, both transverse to tensile test direction, are generated. The average value of such stresses in these planes is about 0.2 times the applied stress, although it can be as high as the order of the applied stress.

Therefore, <110>-textured BCC materials are sensitive *per se* to delamination. In fact it has been said recently that ferritic materials with <110> texture syndrome suffer delamination; however, as has been

reported by Kimura and co-workers [16], one can take advantage of delamination to improve the toughness of the material in some applications.

In summary, the differences in the USE and DBTT observed between LT and LS samples, is a consequence of the different crack-path between crack-arrester and crack-divider geometries. In the crack arrester geometry, the delamination is thought to relax the triaxial stress conditions and to blunt the crack tip. To fracture a material, crack re-initiation is necessary and occurs under conditions of nearly uniaxial tension, which is an unfavorable cleavage. Hence, high absorbed energy is obtainable through the delamination [28] in LS samples.

The P-u curves obtained from instrumented Charpy tests (Figure 8) are very useful to investigate the effect of splitting on the DBTT. Meanwhile the P-u curves of LT samples present similar behavior regardless of the test temperature, P-u curves for LS samples present a peculiar behavior. For LT samples, at which ductile fracture surfaces were observed in Figure 7(a), P gradually decreases after a maximum value P_m is reached. This means that the fracture manner was ductile throughout the impact test. On the other hand, for LS samples, at which extensive delamination was observed in Figures 7(b), P-u curves exhibits a unique behavior. It is observed how P sharply drops after P_m is attained, presenting a sequence of plateaus followed by a sharp drop until P reach zero. Such a plateau region for the impact load results from delamination caused by crack branching. The decrease in P following the plateau region is an effect in which new (micro) cracks were nucleated. This sequence of “steps” resulting from the delamination is also observed in three-point bend test for an ultra-high carbon steel laminate composites [29]. This behavior in LS samples could be explained in basis that once delamination starts, the propagation of the main crack throughout all the sample thickness is inhibited, and then there is no decrease on P without the occurrence of new cracks. In other words, the crack is blunted by delamination. As a result, the absorbed energy becomes larger by the delamination effect. This is particularly significant for the case of test temperature of 75 °C (Figure 7(b)). Moreover, because of the blunted crack by delamination, the sample behaves as an un-notched one during the test.

Conclusions

The anisotropy in the Charpy impact toughness behavior of FeCrAl ODS ferritic alloy PM 2000 was investigated with specific emphasis of fractographic and microstructural features. The results obtained show that:

1. Elongated grains in the rolling direction (GAR≈4) were found. Moreover, a quasi-equiaxial grain (GAR ≈1) with an average diameter of 0.8±0.1 μm are obtained in TS section. A strong texture with RD // <110> and ND // <100> with a dominating {001}<110> component, i.e. the crystallographic plane (100) is parallel to the sheet tube surface, is found. Thus, ductile {110} planes are abundant in TS plane in both LT and LS samples.
2. The reinforcement particles consist of $Y_3Al_5O_{12}$ garnet (YAG) and $YAlO_3$ perovskite (YAP) phases with sizes ranging from 3 nm to 40 nm which are preferentially aligned along grain boundaries. Some stringers of large Y-Al-Ti oxides where found along RD. The weak interfaces between the second oxides located in the grain boundaries enhance the splitting found in both LT and LS samples.
3. The splitting of crack-divider type was observed in LT specimens, whereas crack-arrester type was observed in LS specimens. The differences in crack-type between LS and LT specimens could be related with the plastic anisotropy. Because of the considerably higher plastic deformation in S-direction than in T-direction, the plastic constrain is S-direction would lead to an increase of σ_x in the case of LT samples, and of σ_z in the case of LS sample that would cause delamination perpendicular to notch base for LT samples and parallel to notch base for LS samples.
4. The delamination toughening phenomenon, as introduced by Kimura et al [16], is able to explain the evolution of USE and DBTT observed in LS samples. In the crack arrester geometry of LS samples, the delamination is thought to relax the triaxial stress conditions and to blunt the crack tip. To fracture a material, crack re-initiation is necessary and occurs under conditions of nearly

uniaxial tension, which is an unfavorable cleavage. Hence, high absorbed energy is obtainable through the delamination in LS samples.

5. The differences in the USE and DBTT observed between LT and LS samples, is a consequence of the different crack-path between crack-arrester and crack-divider geometries. In the crack arrester geometry, the delamination is thought to relax the triaxial stress conditions and to blunt the crack tip. To fracture a material, crack re-initiation is necessary and occurs under conditions of nearly uniaxial tension, which is an unfavorable cleavage. Hence, high absorbed energy is obtainable through the delamination in LS samples.

Acknowledgments

PM 2000^{TM} is a trademark of Plansee GmbH. The authors acknowledge the financial support of the Spanish Ministerio de Economia e Innovación (MINECO) in the form of a Coordinate Project in the Energy Area of Plan Nacional 2009 (ENE2009-13766-C04-01). GP acknowledges MINECO for financial support in the form of PhD Research Grant (FPI). This research was supported by ORNL's Shared Research Equipment (SHaRE) User Facility, which is sponsored by the Office of Basic Energy Sciences, US Department of Energy.

References

[1] S. Ukai and M. Fujiwara: J. Nucl. Mater., 2002, vol. 307–311, pp. 749-757.

[2] S. Jitsukawa, A. Kimura, A. Kohyama, R.L. Klueh, A.A. Tavassoli, B. van der Schaaf, G.R. Odette, J.W. Rensman, M. Victoria and C. Petersen: J. Nucl. Mater., 2004, 329–333, pp. 39-46.

[3] M.M. Abu-Khader: Progress in Nuclear Energy, 2009, vol. 51, pp. 225-235.

[4] G.S. Bauer: J. Nucl. Mater., 2010, vol. 398, pp. 19-27.

[5] J. Chen, M.A. Pouchon, A. Kimura, P. Jung and W. Hoffelner: J. Nucl. Mater., 2009, vol. 386-388, pp. 143-146.

[6] S. Ukai, M. Harada, H. Okada, M. Inoue, S. Nomura, S. Shikakura, T. Nishida, M. Fujiwara and K. Asabe: J. Nucl. Mater., 1993, vol. 204, pp. 74–80.

[7] M.J. Alinger, G.R. Odette and G.E. Lucas: J. Nucl. Mater., 2002, vol. 307-311, pp. 484-489.

[8] R. Kasada, N. Toda, K. Yutani, H.S. Cho, H. Kishimoto and A. Kimura: J. Nucl. Mater., 2007, vol. 367-370, pp. 222-228.

[9] C. Capdevila, U. Miller, H. Jelenak and H. Bhadeshia: Mater. Sci. Eng. A, 2001, vol. 316, pp. 161-165.

[10] C. Capdevila, F. G. Caballero and C. G. de Andres: Mater. Sci. Technol., 2003, vol. 19, pp. 581-586

[11] M. Klimiankou, R. Lindau, A. Moslang and J. Schroder: Powder Metall., 2005, vol. 48, pp. 277-287.

[12] M. Klimiankou, R. Lindau and A. Möslang: J. Crystal Growth, 2003, vol. 249, pp. 381-387.

[13] G. Pimentel, I. Toda-Caraballo, J. Chao and C. Capdevila: J. Mater. Sci., 2012, vol. 47, pp. 5605-5616.

[14] N. Tsuji, S. Okuno, Y. Koizumi and Y. Minamino: Mater. Trans., 2004, vol. 45, pp. 2272-2281.

[15] R. Song, D. Ponge and D. Raabe: Acta Mater., 2005, vol. 53, pp. 4881-4192.

[16] Y. Kimura, T. Inoue, F. Yin and K. Tsuzaki: ISIJ Int., 2010, vol. 50, pp. 152-161.

[17] J. D. Embury, N. J. Petch, A. E. Wraith and E. S. Wright: Trans. Metall. Soc. AIME, 1967, vol. 239, pp. 114-132.

[18] D. W. Kum, T. Oyama, J. Wadsworth and O. D. Sherby: J. Mech. Phys., 1983, vol. 31, pp. 173-186.

[19] Y. Kimura: Bull. Iron Steel Inst. Jpn., 14 (2009), 154.

[20] R. Hill: The mathematical theory of plasticity, The Clarendon Press, Oxford, 1950, 254.

[21] P. Brozzo andG. Buzzichelli: Scr. Metall., 1976, vol. 10, pp. 235-240

[22] C. M. Yen and C. A. Stickels: Metall. Trans., 1970, vol. 1, pp. 3037-3047.

[23] W. Zhou and N. L. Loh: Scr. Mater., 1996, vol. 34, pp. 633-639.

[24] N. Yu. Zolotorevsky and N. Yu. Krivonosova: Mater. Sci. Eng. A, 1996, vol. 205, pp. 239-246.

[25] E.C. Oliver, M.R. Daymond and P.J. Withers: Acta Mater., 2004, vol. 52, pp. 1937-1951.

[26] J. Gil Sevillano, J. Alkorta, D. González, S. Van Petegem, U. Stuhr and H. Van Swygenhoven: Adv. Eng. Mater., 2008, vol. 10, pp. 951-954.

[27] W. F. Hosford: "The mechanics of crystals and textured polycrystals", Oxford University Press, New York, USA, 1993, 152.

[28] M. Taguchi, H. Sumitomo, R. Ishibashi and Y. Aono : Mater. Trans., 2008, vol. 49, pp. 1303-1310.

[29] M. Pozuelo, F. Carreno, and O.A. Ruano: Compos. Sci. Technol., 2006, vol. 66, pp. 2671–76.

Figures

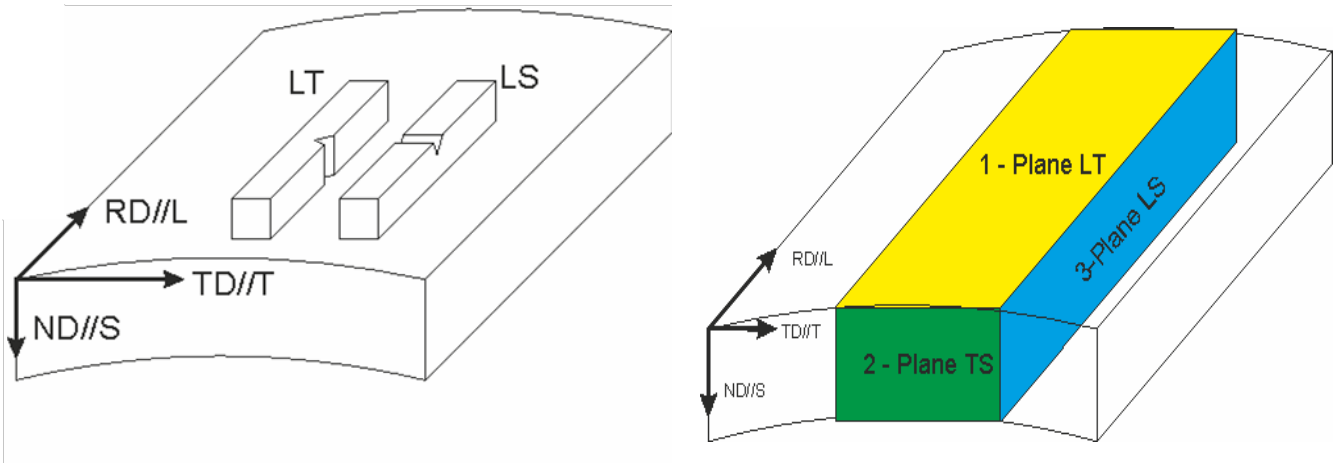

(a) (b)

Figure 1.- Scheme indicating the position of the notch respect to the rolling direction for PMT material, and Scheme of sectioned samples for EBSD measurements, respectively.

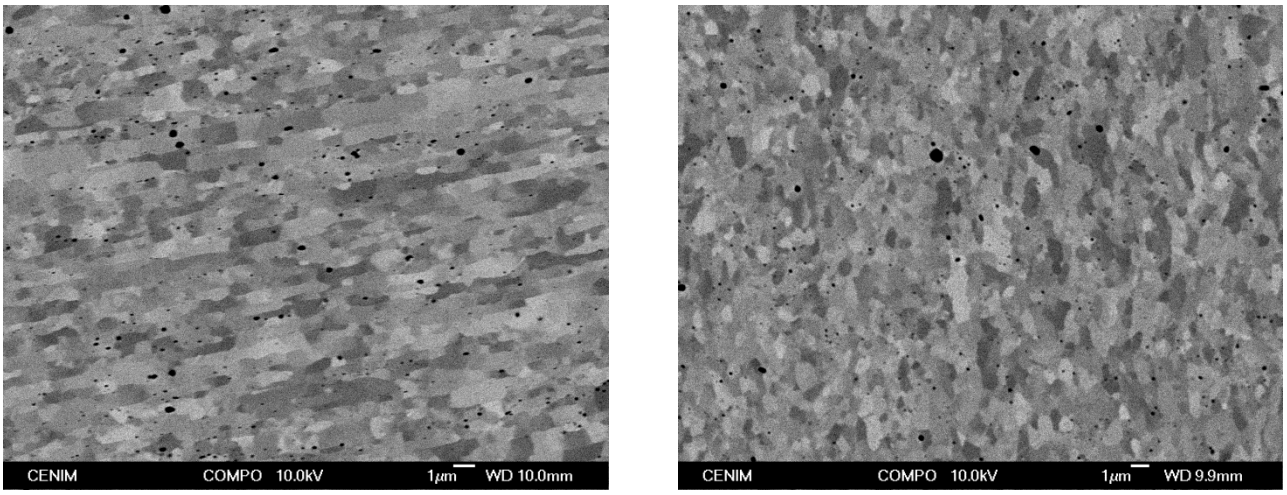

(a) (b)

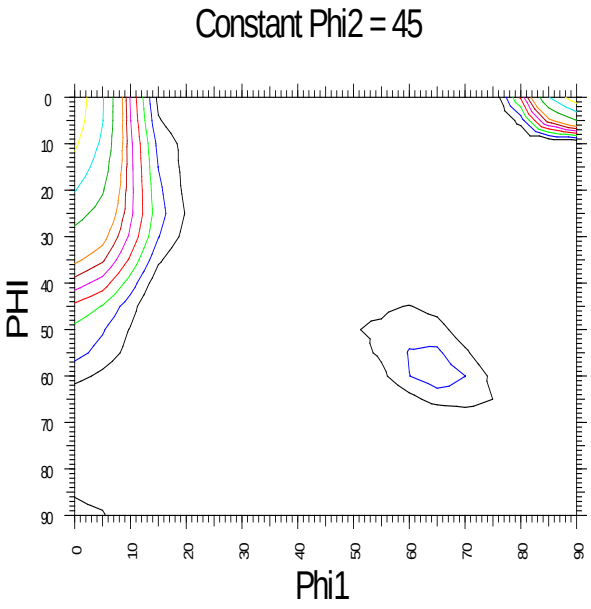

(c)

Figure 2. BS-SEM images of PMT samples: (a) LT and (b) TS planes. ODF cut at ϕ2 = 45° is shown in (c)

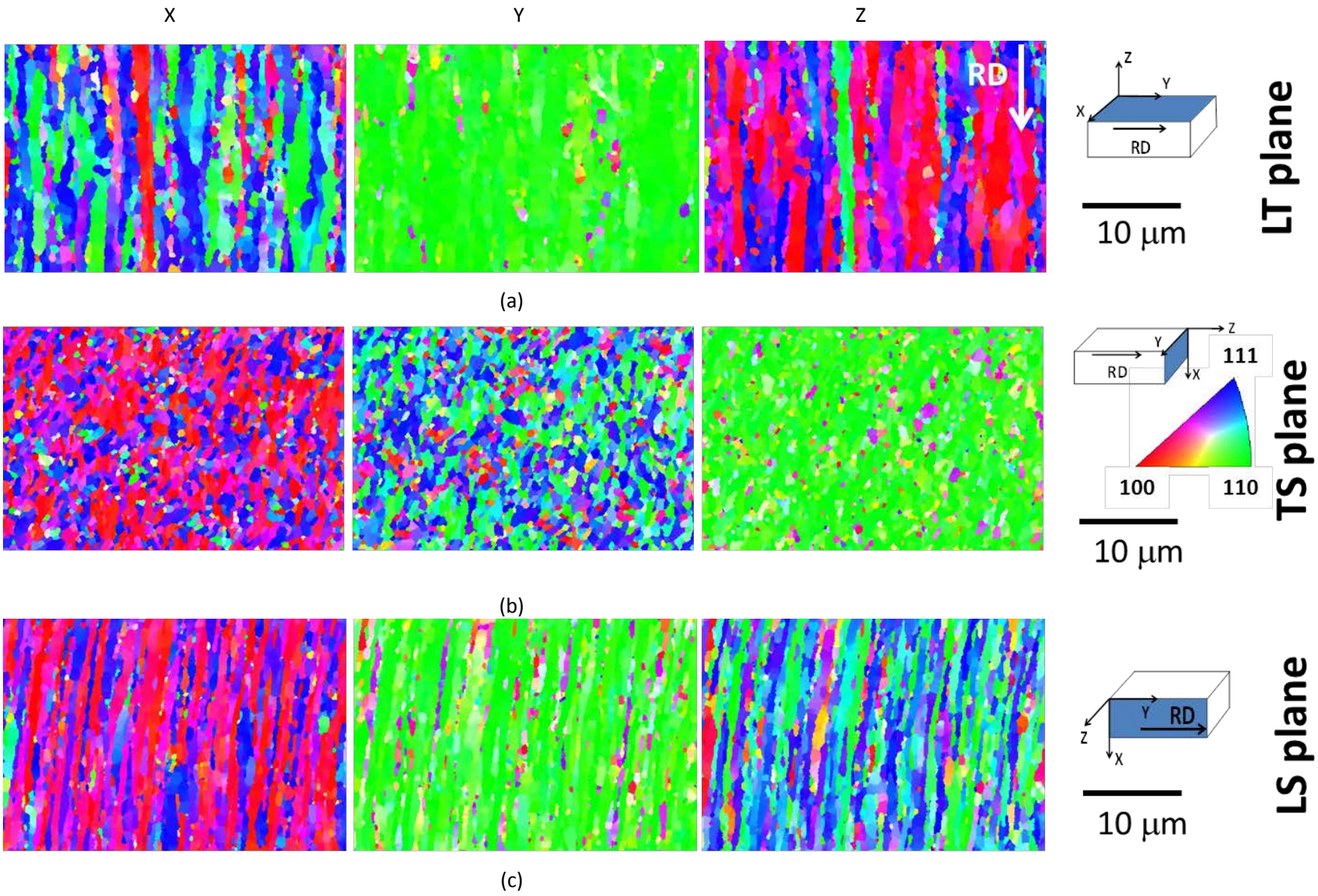

Figure 3. IPF maps of PMT samples in the (a) LT, (b) LT, and (c) LS sections as labeled in Figure 1.

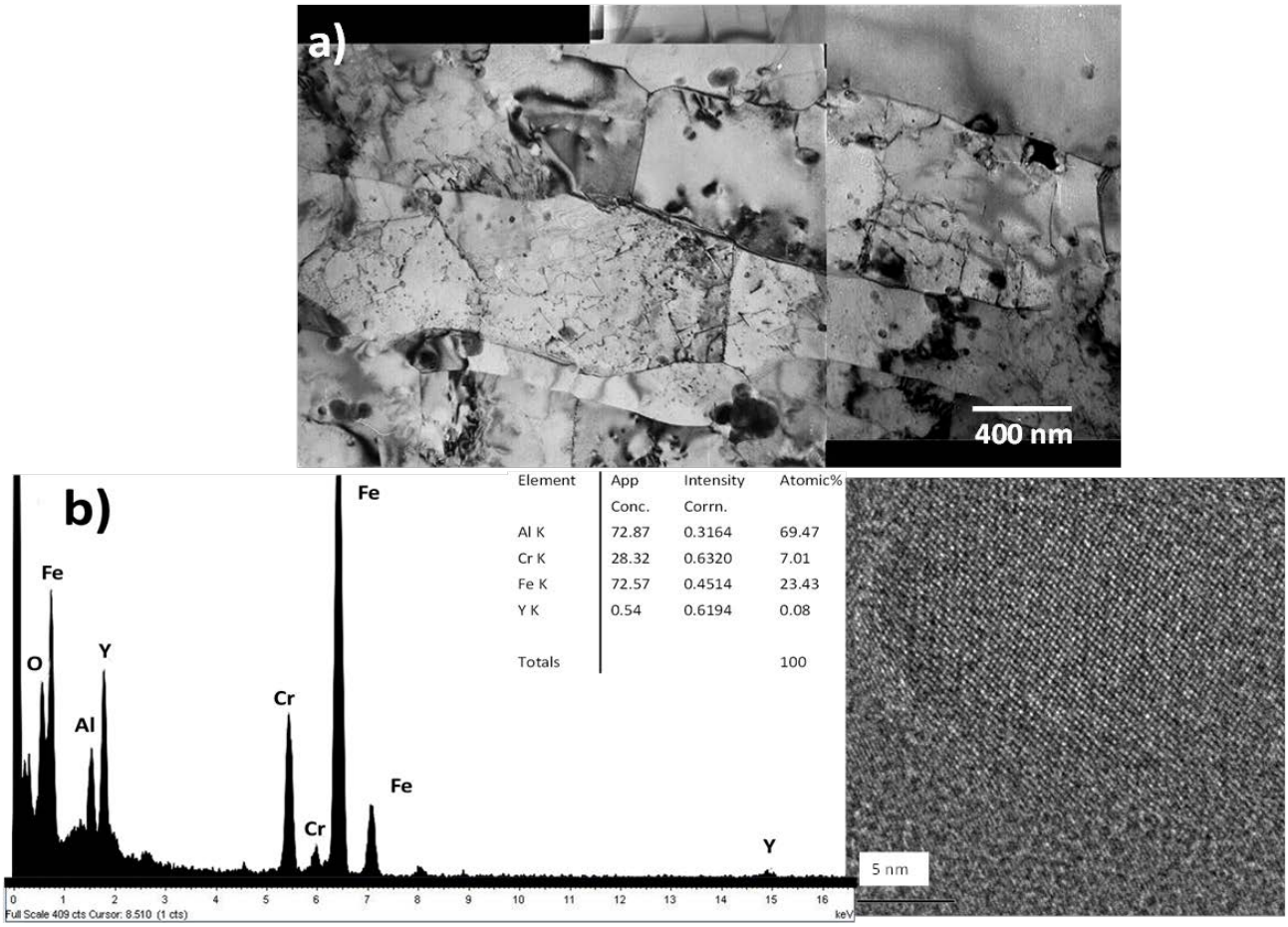

Figure 4. (a) BF TEM image of LS section indicating the alignment of oxide particles on the grain boundary, (b) nature and size of oxide particles.

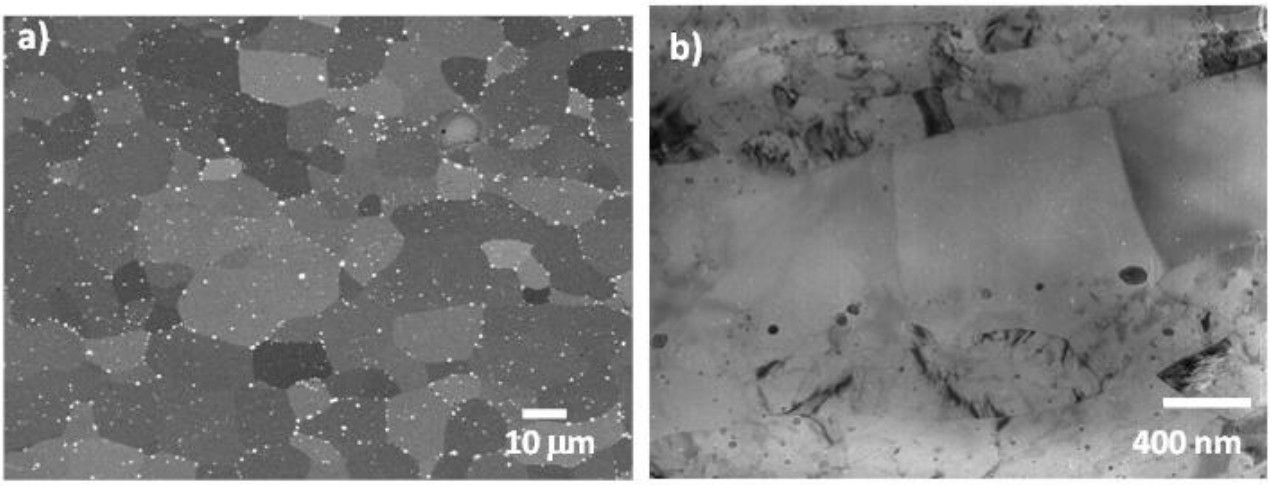

Figure 5. (a) back-scattered SEM of grain boundary particles (in white) in TS plane, and (b) TEM in LS plane.

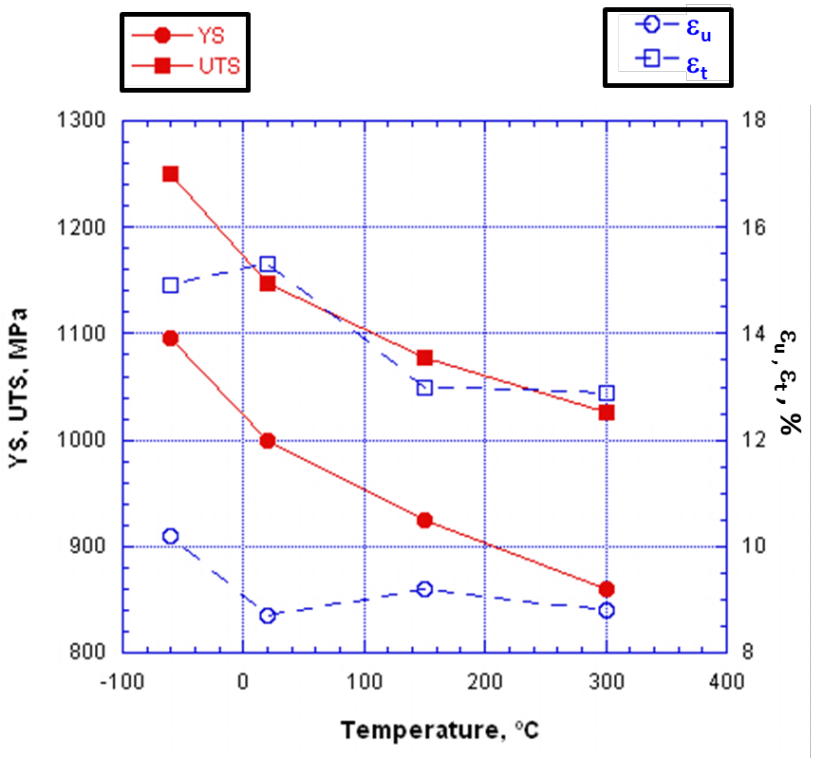

(a)

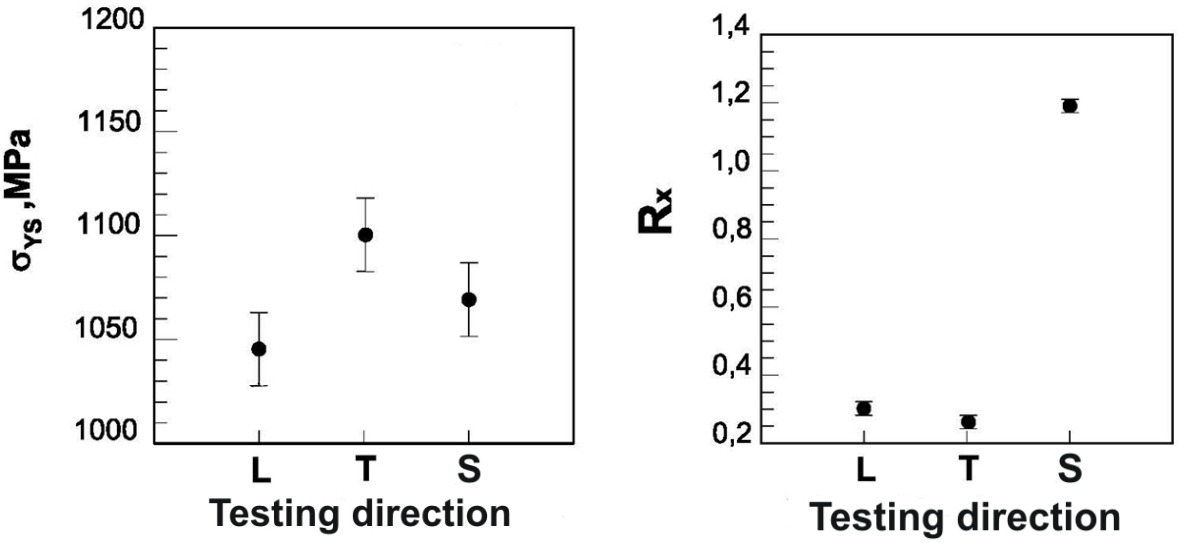

(b)

Figure 6. Evolution of (a) YS, UTS, ε_t, and ε_u with testing temperature resulting from tensile tests for PMT samples, and (b) YS and R_X for L, T and S direction from compression test at room temperature.

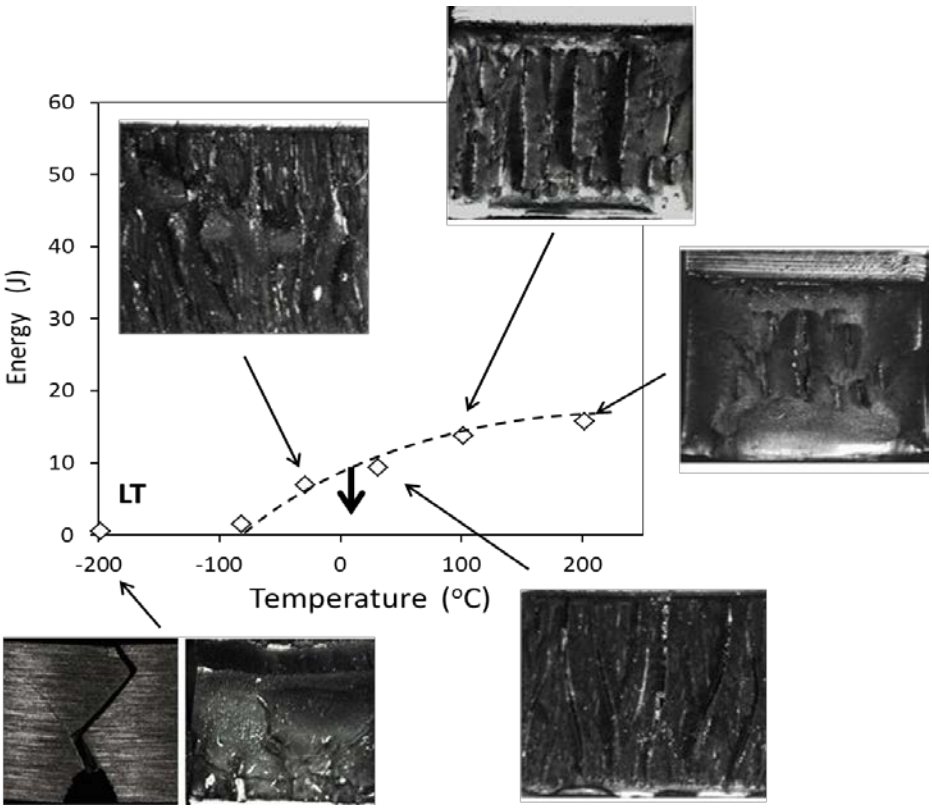

(a)

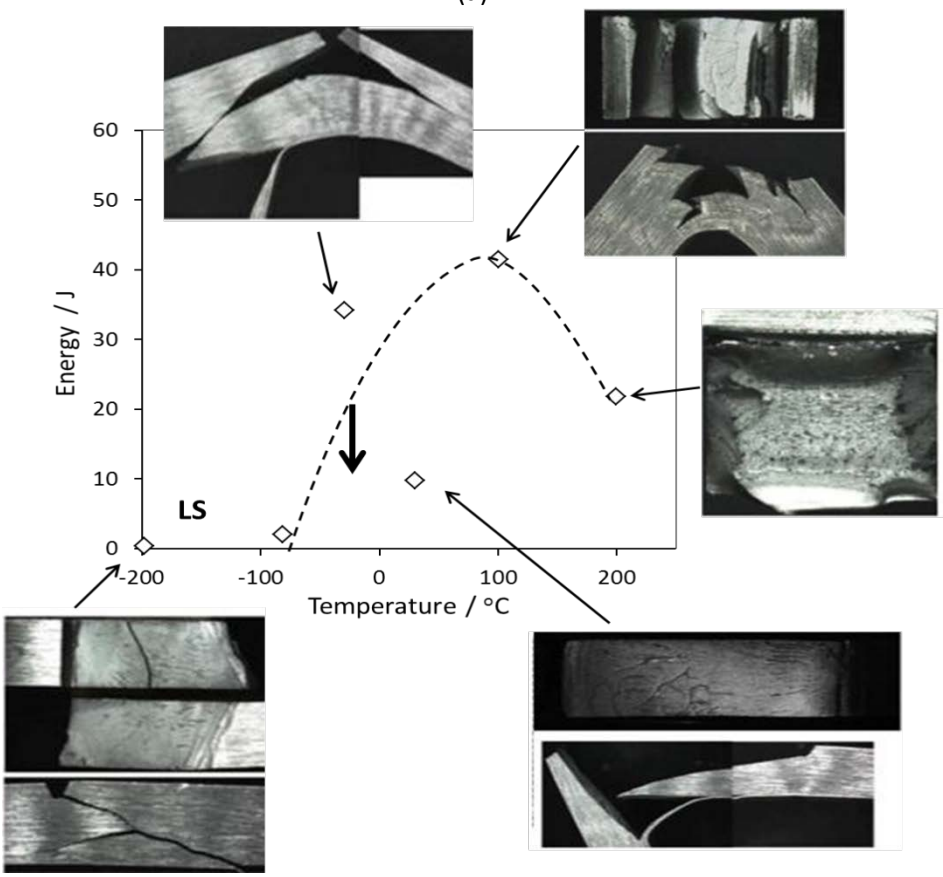

(b)

Figure 7. Charpy Impact energy of the PMT samples for (a) LT specimens and (b) LS specimens

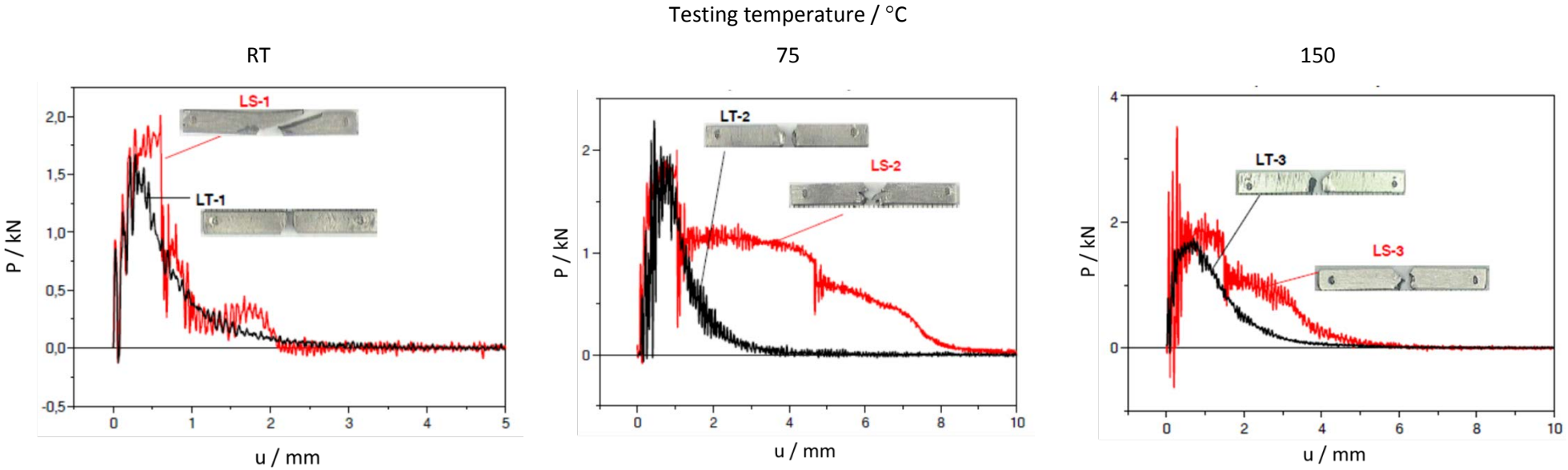

Figure 8. Relations between load and deflection during Charpy impact tests for LS and LT samples with different test temperatures and appearance of samples after tests.

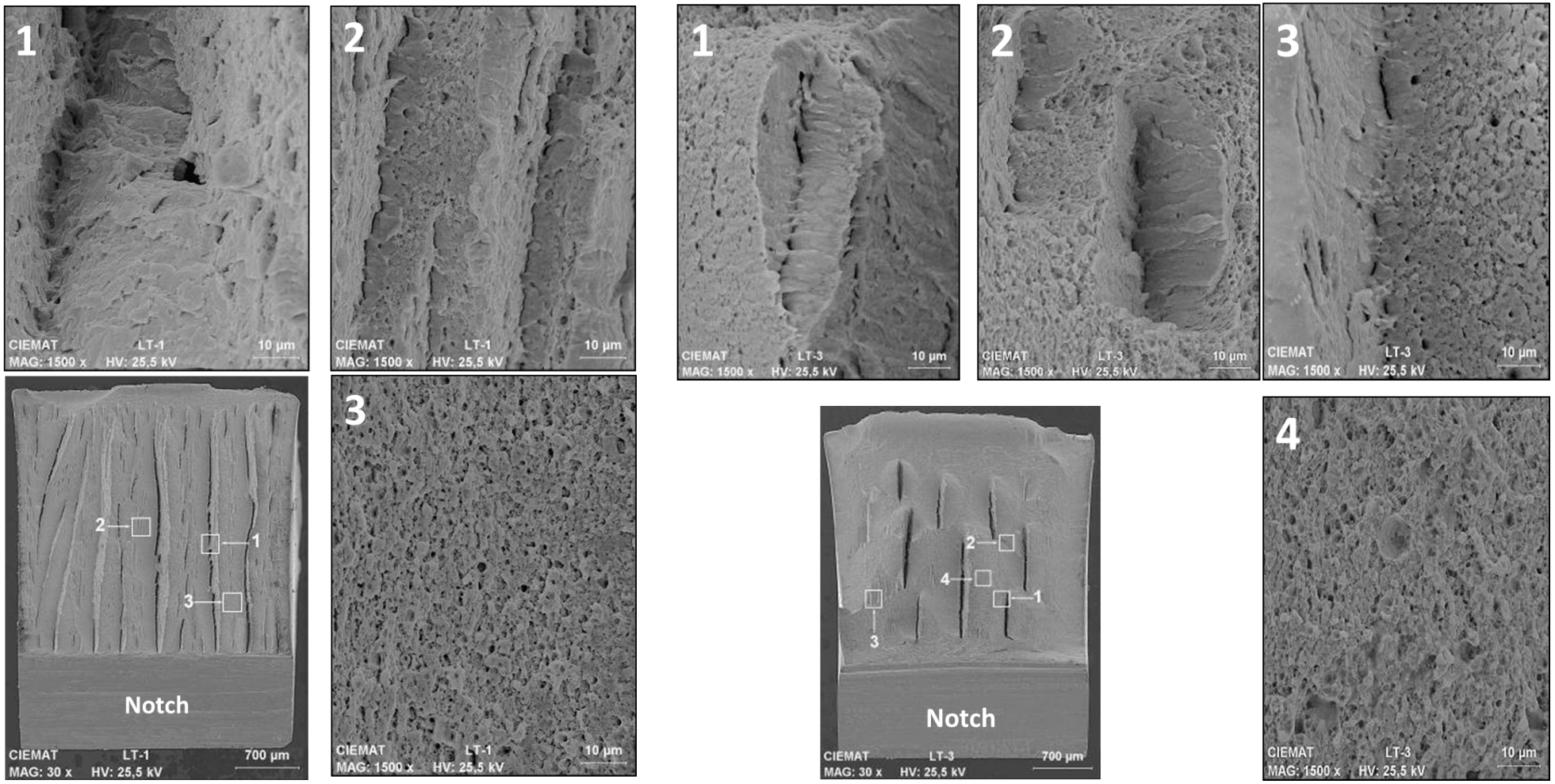

Figure 9. Fracture morphology of LT specimen tested at (a) RT and (b) 150 °C. SEM micrographs show details of the splitting observed in the fracture surface

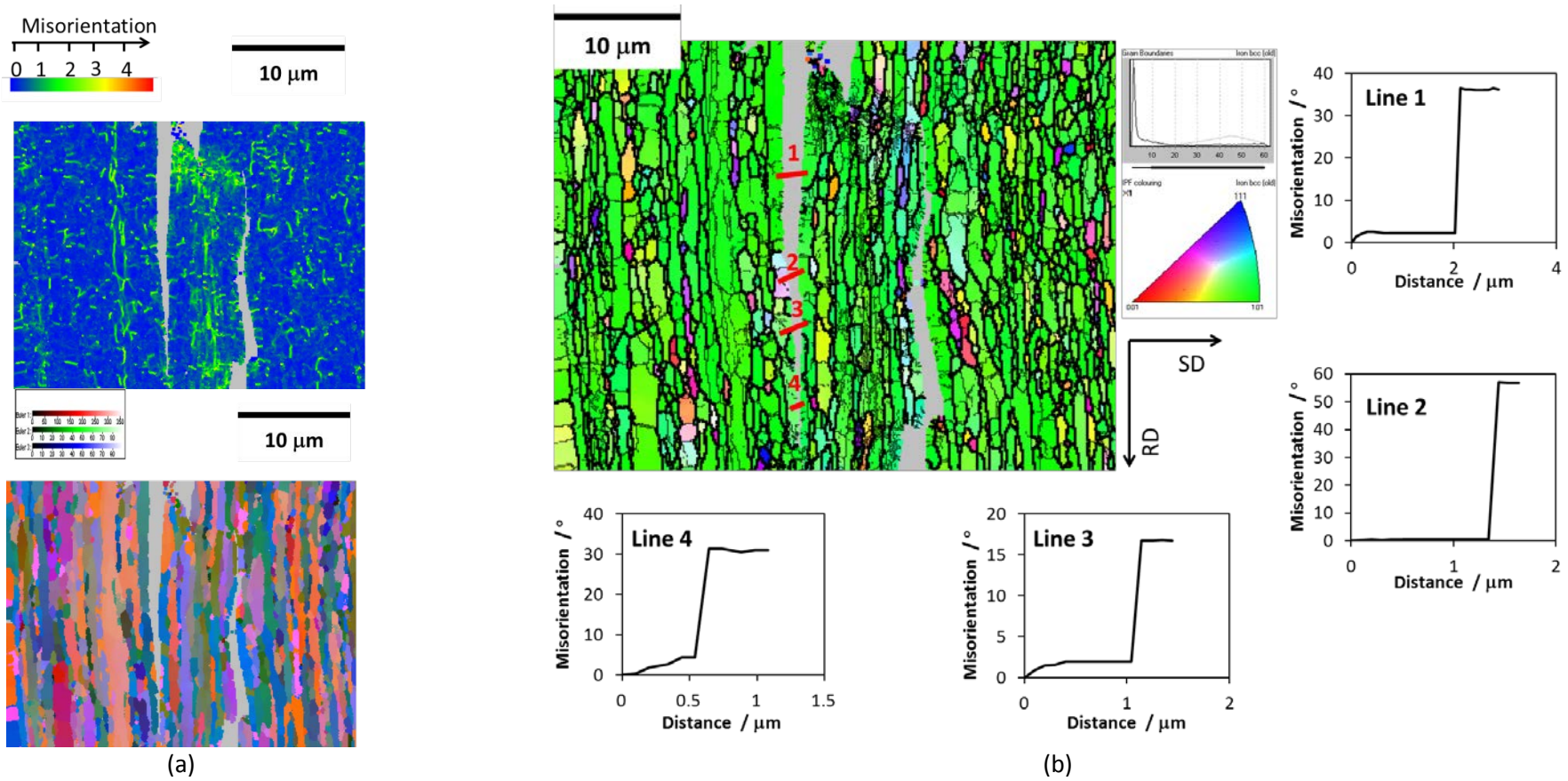

Figure 10. (a) Kernel and Euler angle map and (b) misorientation analysis through lines across the crack in LT sample tested at room temperature. RD stands for rolling direction and SD for striking direction

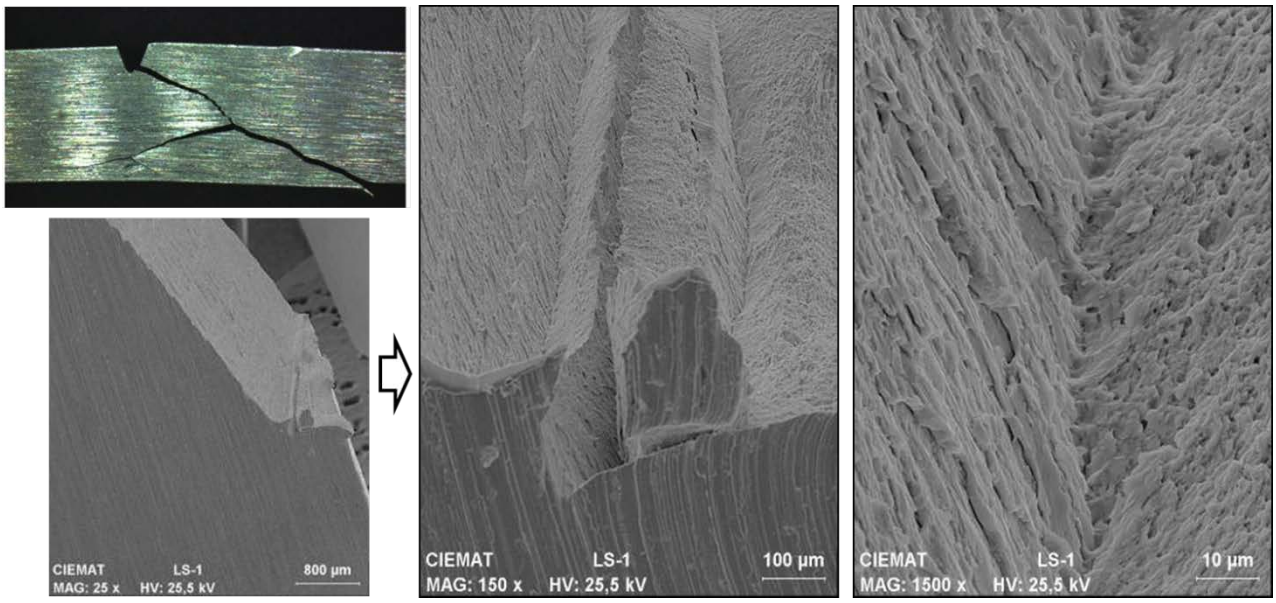

Figure 11. Fracture morphology of LS specimen tested at RT. SEM micrographs show details of 70° fracture plane, and ramification close to the notch

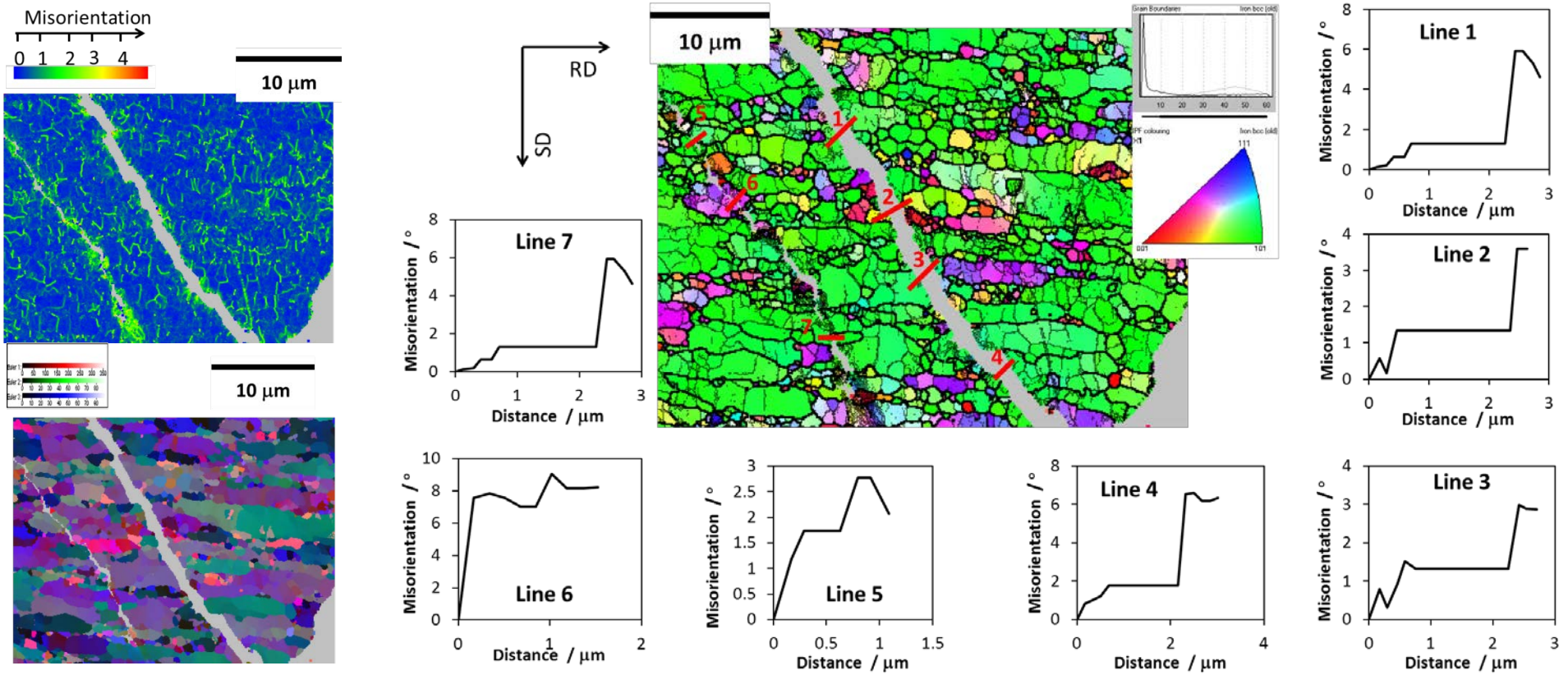

Figure 12. (a) Kernel and Euler angle map and (b) misorientation analysis through lines across the crack in LT sample tested at -196 °C. RD stands for rolling direction and SD for striking direction

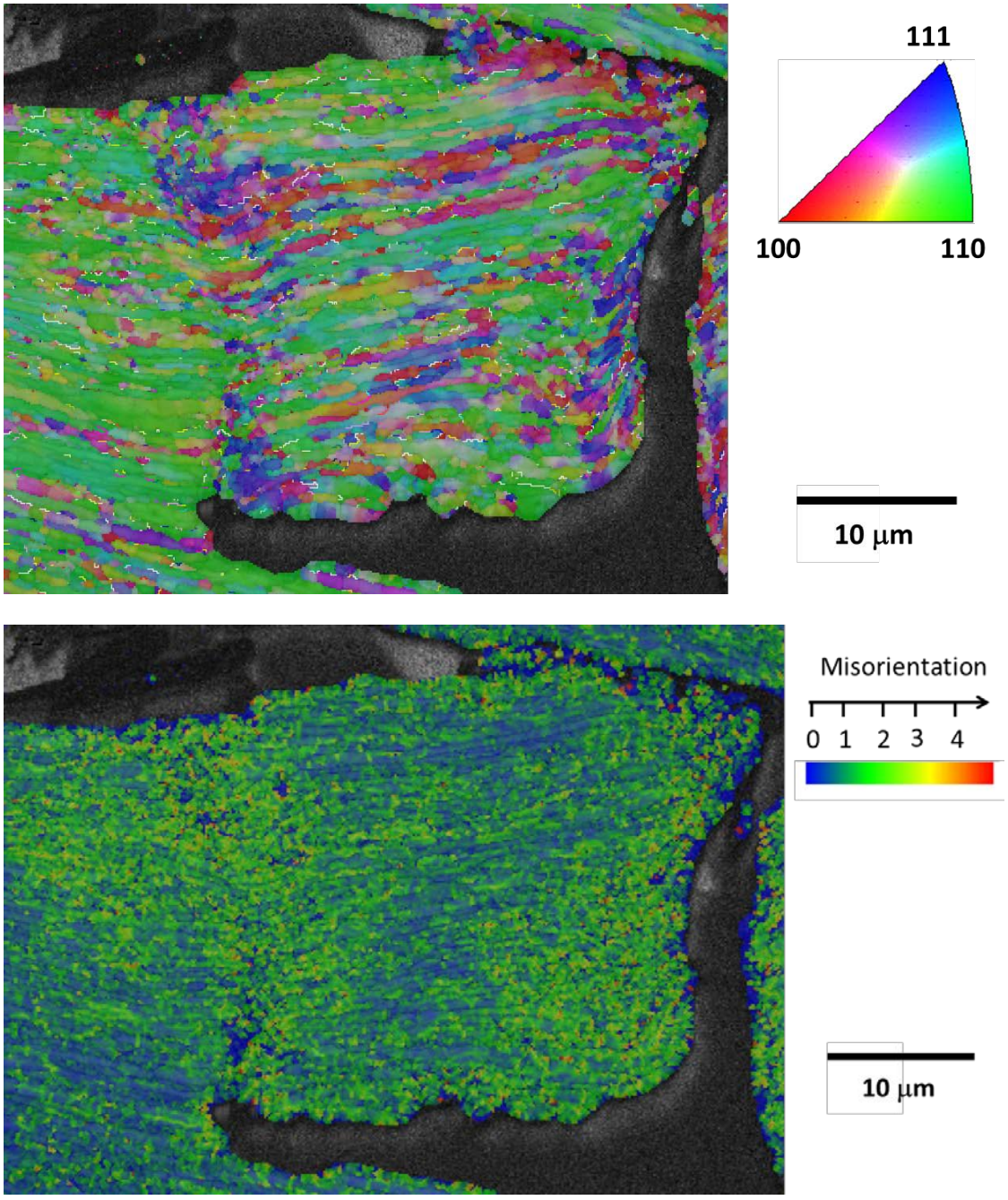

Figure 13. IPF and kernel map illustrating a ductile crack in LS sample tested at 100 °C.

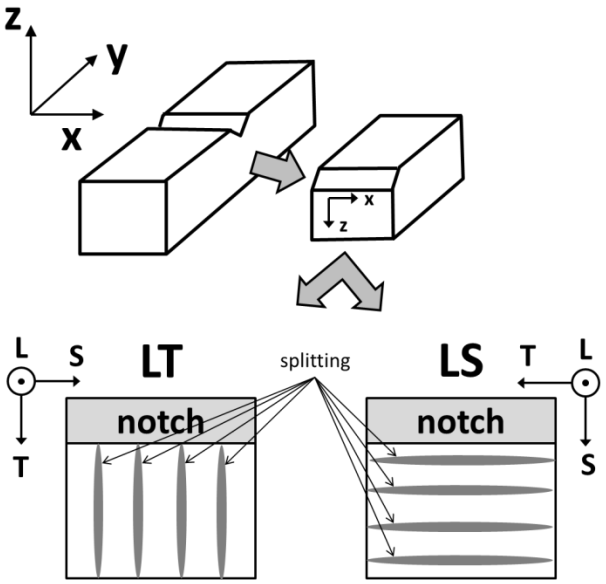

Figure 14. Schematic illustration showing laminate splitting geometries found in LT and LS samples tested according with Cartesian x,y,z and L,T,S (Figure 1(a)) reference systems.